

Photodissociation dynamics of the simplest alkyl peroxy radicals, CH_3OO and $\text{C}_2\text{H}_5\text{OO}$, at 248 nm

Erin N. Sullivan, Bethan Nichols, and Daniel M. Neumark

Citation: *The Journal of Chemical Physics* **148**, 044309 (2018);

View online: <https://doi.org/10.1063/1.5011985>

View Table of Contents: <http://aip.scitation.org/toc/jcp/148/4>

Published by the [American Institute of Physics](#)

Articles you may be interested in

Channel branching ratios in CH_2CN^- photodetachment: Rotational structure and vibrational energy redistribution in autodetachment

The Journal of Chemical Physics **147**, 234309 (2017); 10.1063/1.5001475

Imaging spectroscopy of the missing REMPI bands of methyl radicals: Final touches on all vibrational frequencies of the 3p Rydberg states

The Journal of Chemical Physics **148**, 014303 (2018); 10.1063/1.5011797

Editorial: JCP Communications—Updating a valued community resource

The Journal of Chemical Physics **148**, 010401 (2018); 10.1063/1.5019731

Sub-Doppler slit jet infrared spectroscopy of astrochemically relevant cations: Symmetric (ν_1) and antisymmetric (ν_6) NH stretching modes in ND_2H_2^+

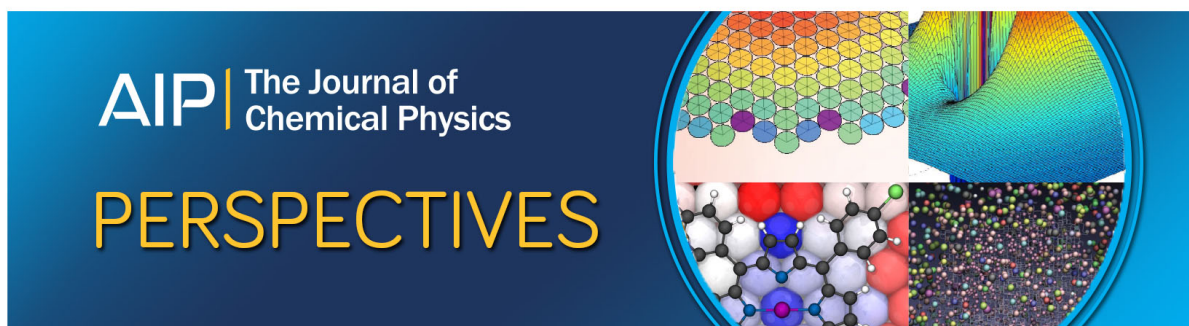
The Journal of Chemical Physics **148**, 014304 (2018); 10.1063/1.5003230

CRF-PEPICO: Double velocity map imaging photoelectron photoion coincidence spectroscopy for reaction kinetics studies

The Journal of Chemical Physics **147**, 013944 (2017); 10.1063/1.4984304

Potential energy surfaces for $\text{O} + \text{O}_2$ collisions

The Journal of Chemical Physics **147**, 154312 (2017); 10.1063/1.4997169



Photodissociation dynamics of the simplest alkyl peroxy radicals, CH₃OO and C₂H₅OO, at 248 nm

Erin N. Sullivan, Bethan Nichols, and Daniel M. Neumark^{a)}

Department of Chemistry, University of California, Berkeley, California 94720, USA and Chemical Sciences Division, Lawrence Berkeley National Laboratory, Berkeley, California 94720, USA

(Received 3 November 2017; accepted 10 January 2018; published online 26 January 2018)

The photodissociation dynamics of the simplest alkyl peroxy radicals, methyl peroxy (CH₃OO) and ethyl peroxy (C₂H₅OO), are investigated using fast beam photofragment translational spectroscopy. A fast beam of CH₃OO⁻ or C₂H₅OO⁻ anions is photodetached to generate neutral radicals that are subsequently dissociated using 248 nm photons. The coincident detection of the photofragment positions and arrival times allows for the determination of mass, translational energy, and angular distributions for both two-body and three-body dissociation events. CH₃OO exhibits repulsive O loss resulting in the formation of O(¹D) + CH₃O with high translational energy release. Minor two-body channels leading to OH + CH₂O and CH₃O + O(³P) formation are also detected. In addition, small amounts of H + O(³P) + CH₂O are observed and attributed to O loss followed by CH₃O dissociation. C₂H₅OO exhibits more complex dissociation dynamics, in which O loss and OH loss occur in roughly equivalent amounts with O(¹D) formed as the dominant O atom electronic state via dissociation on a repulsive surface. Minor two-body channels leading to the formation of O₂ + C₂H₅ and HO₂ + C₂H₄ are also observed and attributed to a ground state dissociation pathway following internal conversion. Additionally, C₂H₅OO dissociation yields a three-body product channel, CH₃ + O(³P) + CH₂O, for which the proposed mechanism is repulsive O loss followed by the dissociation of C₂H₅O over a barrier. These results are compared to a recent study of *tert*-butyl peroxy (*t*-BuOO) in which 248 nm excitation results in three-body dissociation and ground state two-body dissociation but no O(¹D) production. Published by AIP Publishing. <https://doi.org/10.1063/1.5011985>

I. INTRODUCTION

Alkyl peroxy radicals (RO₂) are important intermediates that are crucial to atmospheric and combustion chemistry processes.^{1,2} In the atmosphere, RO₂ can interact with the NO_x cycle to contribute to the production of ozone in the troposphere.^{1,3} In low temperature autoignition processes, alkyl peroxy radicals are of interest due to their ability to isomerize to QOOH, a species in which the unpaired electron sits on a carbon of the alkyl group, as opposed to the terminal oxygen atom. QOOH readily decomposes to several product channels that propagate low-temperature hydrocarbon oxidation processes.^{2,4} Photodissociation experiments provide unique insights into how alkyl peroxy radicals dissociate on their excited and ground electronic states, as shown in our recent experiments on the *t*-butyl peroxy radical (*t*-BuOO).⁵ Characterizing how these dynamics depend on the alkyl substituents is crucial to gaining an insight into the general reactivity of peroxy radicals and how they participate in larger chemical arenas. To this end, we investigate the photodissociation of CH₃OO and C₂H₅OO at 248 nm in this work.

In previous work, the UV absorption spectra of CH₃OO and C₂H₅OO have been measured and found to have broad features that peak near 240 nm that are attributed to the

$\tilde{B}^2A'' \leftarrow \tilde{X}^2A''$ transition, similar to other alkyl peroxy radicals.⁶⁻⁹ Infrared spectra of both species have been obtained via matrix isolation spectroscopy.^{10,11} Step-scan Fourier transform spectroscopy has been used to obtain temporally resolved IR spectra for CH₃OO, identifying major absorption bands and characterizing the torsional splitting of the ν_1 , ν_2 , and ν_9 modes.¹²⁻¹⁴ Blanksby *et al.*¹⁵ have reported the photoelectron (PE) spectra of the CH₃OO⁻ and C₂H₅OO⁻ anions, finding the electron affinities of the corresponding radicals to be 1.161 ± 0.005 eV and 1.186 ± 0.004 eV, respectively. The $\tilde{A} \leftarrow \tilde{X}$ electronic transitions of CH₃OO and C₂H₅OO in the near-IR absorption region have been characterized by Miller and co-workers¹⁶⁻¹⁸ using cavity ringdown spectroscopy. For both radicals, ground state and \tilde{A} state rovibronic structures were observed and identified. Additionally, for the C₂H₅OO species, symmetry differences allowed for distinguishing the *trans* and *gauche* configurations of the radical using rotational contours. Finally, photoionization studies of both neutral radicals have been performed, yielding an adiabatic ionization energy of CH₃OO (10.33 ± 0.05 eV) and a CH₃⁺-OO bond energy of 80 ± 7 kJ/mol.¹⁹ This work also showed that the C₂H₅OO⁺ cation is destabilized and can easily dissociate into ground state fragments. For this reason, very few C₂H₅OO⁺ cations were observed and the ionization energy of C₂H₅OO was not determined.

The products from ultraviolet photolysis of CH₃OO and C₂H₅OO in Ar + O₂ matrices at 254 nm were characterized

^{a)}Author to whom correspondence should be addressed: dneumark@berkeley.edu

using infrared spectroscopy. For CH_3OO , the major products were identified as HO_2 , CH_2O , CO , CO_2 , and H_2O .¹¹ For $\text{C}_2\text{H}_5\text{OO}$, similar products were observed, namely, CO , CO_2 , and H_2O , in addition to a major band in the spectrum that was attributed to the formation of CH_3CHO .¹⁰

Gas phase photodissociation experiments on CH_3OO at 248 nm have reported the formation of $\text{CH}_3\text{O}(\tilde{X}^2E)$, $\text{OH}(\tilde{X}^2\Pi)$, and $\text{OH}(\tilde{A}^2\Sigma^+)$ via laser induced fluorescence and emission spectroscopy.^{20,21} The authors suggested that the formation of the OH radicals resulted from dissociation following isomerization to QOOH .²⁰ Based on quantum yield calculations that showed relatively low yields of the observed $\text{OH} + \text{CH}_2\text{O}$ and $\text{O} + \text{CH}_3\text{O}$ channels, the authors proposed that $\text{O}_2 + \text{CH}_3$ was the dominant dissociation channel, although experimental evidence for this was not presented.²⁰

While no gas phase photodissociation experiments on $\text{C}_2\text{H}_5\text{OO}$ have been reported previously, such experiments have been carried out on simpler and more complex peroxy radicals than those considered here, namely, HO_2 and *t*-BuOO. At a dissociation wavelength of 220 nm, $\text{OH} + \text{O}(\tilde{1}D)$ was the primarily observed channel from HO_2 , making up 84% of the products, with about 16% from $\text{OH} + \text{O}(\tilde{3}P)$.²² The OH fragment was found to contain very little internal energy, and thus, the authors related the experimental results to an impulsive model in which the O–O bond is cleaved repulsively. Recent work in our group considered the photodissociation of the *t*-BuOO radical at 248 nm,⁵ for which the dominant photoproducts were $\text{O}(\tilde{3}P) + \text{CH}_3 + \text{acetone}$ with minor contributions from two-body O_2 and HO_2 loss. The three-body dissociation products were proposed to form via repulsive cleavage of the O–O bond on the excited state, followed by rapid fragmentation of the remaining *t*-butoxy fragment. Branching ratios and translational energy distributions for two-body dissociation were consistent with O_2 and HO_2 loss occurring statistically on the ground electronic state, indicating that some internal conversion to the ground state occurred prior to dissociation.

As both the smallest (HO_2) and highly substituted (*t*-BuOO) peroxy radicals have been studied in some depth, the question remains as to how small alkyl substituents affect the photodissociation dynamics of this class of radicals. Ground state potential energy surfaces for the two simplest alkyl peroxy radicals, CH_3OO ^{23–31} and $\text{C}_2\text{H}_5\text{OO}$,^{23,25,31–45} are depicted in Figs. 1 and 2. These plots show the possible dissociation product channels (labeled in blue) and their energetics. Several two-body and three-body channels are accessible for both radicals when photoexcited at 248 nm (purple arrows).

In this work, the photodissociation dynamics of CH_3OO and $\text{C}_2\text{H}_5\text{OO}$ excited at 248 nm are investigated via fast radical beam photofragment translational spectroscopy. For CH_3OO dissociation, channel 1A is the predominant photofragment mass channel detected with $\text{O}(\tilde{1}D)$ as the primary electronic state of the O atom; the measured photofragment translational and angular distributions indicate that this channel proceeds via a repulsive excited state. Channel 3A and the three-body channel 4A are also observed as minor channels.

Five product channels are observed for the photodissociation of $\text{C}_2\text{H}_5\text{OO}$. The dominant two-body channels are channel 1B and an OH loss channel (6B or 7B or some combination thereof) that contribute roughly equally to the photofragment

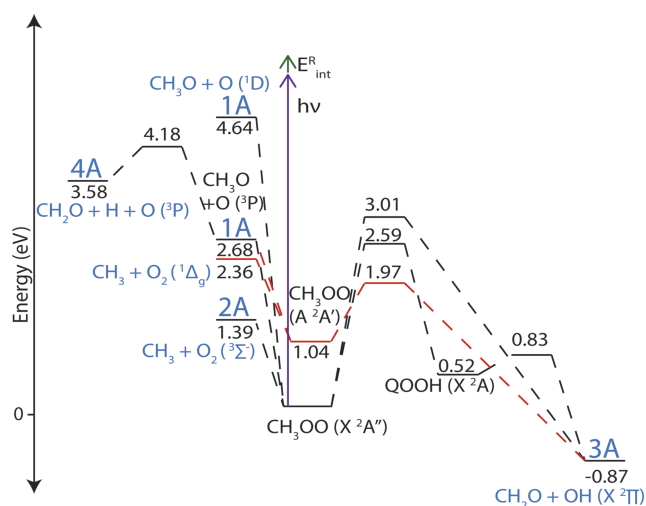


FIG. 1. Potential energy surface for CH_3OO in which product asymptotic energies were determined using experimental heats of formation while transition state energies and structures were taken from Ref. 30. The red portion depicts pathways on the \tilde{A} state surface. Geometries were optimized using B3LYP/6-311G(d,p), and energies were calculated using the G2M method for all structures except those leading to channel 4A formation. Information regarding channel 4A was acquired from Ref. 24 in which the energies were calculated using MP3/6-31G** and the geometries optimized using UHF 6-31G**. Product mass channels are defined in blue. The purple arrow represents the energy of a 248-nm photon, 5.00 eV, and the green arrow represents the energy of E_{int}^R , 0.28 eV.

yield. Channels 3B and 5B are documented as minor two-body channels, and their formation is attributed to statistical dissociation following internal conversion to the ground state. The three-body channel 4B is also detected with a translational energy distribution peaking near the maximum available

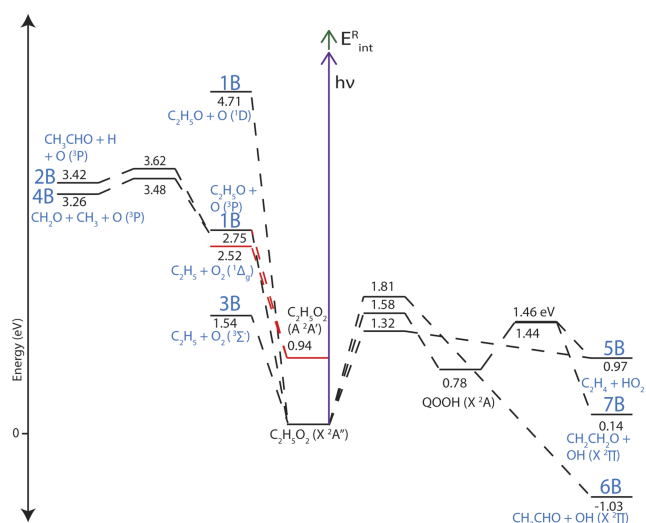


FIG. 2. Potential energy surface for $\text{C}_2\text{H}_5\text{OO}$ in which product asymptotic energies were determined using experimental heats of formation, while transition state energies and geometries were taken from Ref. 41. Geometries were optimized using DFT//B3LYP/6-31G(d,p) and energies were calculated at CBS-Q//B3LYP/6-31G(d,p) for all structures except transition states leading to channels 2B and 4B formation. These transition state structures were taken from Ref. 46 calculated at QCISD(T)/6-311+G(3df,2p). The \tilde{A} state surface is shown in red and was obtained from Ref. 37. Product channel numbers are shown in blue. The purple arrow represents the energy of a 248-nm photon, 5.00 eV, and the green arrow represents the energy of E_{int}^R , 0.28 eV.

energy. This channel is attributed to repulsive O loss, followed by the dissociation of C_2H_5O over a barrier.

II. EXPERIMENTAL METHOD

Methyl hydroperoxide and its partially deuterated isotopolog, CD_3OOH , were synthesized following the procedure cited by Vaghjani and Ravishankara.⁴⁷ In brief, dimethyl sulfate (10 g, 0.079 mol, Sigma Aldrich), 30% hydrogen peroxide (15 mL, Fisher Scientific), and water (25 mL) were stirred at 273 K, while 40% KOH (8.41 g in 12.6 mL of water, Fisher Scientific) was added dropwise over a period of 40 min. The solution was neutralized, the non-deuterated hydroperoxide was extracted into deuterated chloroform, and its NMR spectrum was acquired. This spectrum peaks at 8.26 ppm and 3.19 ppm, matching what has been seen previously in the literature for CH_3OOH .⁴⁷ Our NMR spectrum is found in the [supplementary material](#) (Fig. S1). Deuterated-methyl hydroperoxide and ethyl hydroperoxide were made analogously using d_6 -dimethyl sulfate (Sigma Aldrich) and diethyl sulfate (Sigma Aldrich), respectively. The ethyl hydroperoxide synthesis required about 9 h of reaction time. Further purification and concentration were not necessary.

The fast radical beam machine has been discussed in detail previously.^{48,49} A gaseous mixture of 20 psi He bubbled through a solution of alkyl hydroperoxide (ROOH) (5%-6% in H_2O) was expanded into a vacuum chamber through an Amsterdam piezovalve^{50,51} operating at 100 Hz and a DC grid discharge, producing RO_2^- ions. The ions were accelerated to 6-8 keV and mass-selected using a Bakker-type beam modulation time-of-flight mass spectrometer.^{52,53} The fundamental (1064 nm) of an Nd:YAG laser (Litron LPY742-100) or tunable radiation (700 nm) from a Nd:YAG pumped dye laser (Litron LPY742-100 and Radiant Dyes NarrowScan) intersected the beam of ions, photodetaching an electron to form neutral RO_2 radicals.

To aid in characterizing the neutral radicals formed, photoelectron (PE) spectra of the anions were measured using a spectrometer that sits orthogonal to the direction of the molecular beam.⁴⁹ Detached electrons were accelerated using a velocity-map imaging setup and detected with a chevron-mounted pair of microchannel plates coupled to a phosphor screen (Beam Imaging Solutions BOS-75) and CCD camera. Images were analyzed using the BASEX algorithm,⁵⁴ yielding electron kinetic energy (eKE) distributions from which the vibrational temperature and excitations in the neutral radical were characterized.

Downstream of the PE spectrometer, any remaining anions in the fast beam were deflected, and the neutral RO_2 radicals were dissociated using 248 nm photons from a GAM EX-50 excimer laser. The photofragments were collected in coincidence via a Roentdek Hex80 delay-line anode detector,^{55,56} yielding arrival times and positions for all neutral fragments. The time-and-position sensitive data were used to determine masses, translational energy release, and scattering angle θ of dissociated products for each dissociation event. A beam block of 2.5 mm radius in front of the detector blocked any non-dissociated neutral radicals. To correct for photofragments with low recoil energy hitting this beam block, or

for high translational energy fragments scattering beyond the detector and going undetected, translational energy distributions presented in this work incorporate a detector acceptance function (DAF).⁴⁸

From this information, the two-body translational energy and angular distributions for each mass channel were constructed according to the following:

$$P(E_T, \theta) = P(E_T) \cdot [1 + \beta(E_T)P_2(\cos \theta)], \quad (1)$$

in which β is the energy-dependent anisotropy parameter and $P_2(\cos \theta)$ is the second Legendre polynomial.⁵⁷ The value of β is determined directly from the angular distributions for three-body dissociation. For our experiment, in which the laser is unpolarized, θ is defined as the angle between the laser propagation direction and the recoil axis of dissociation for two-body dissociation events or the normal to the plane of dissociation for three-body events. The value of β in Eq. (1) is $-1/2$ times the value one would obtain in an experiment using linearly polarized light and thus ranges from values of -1 to $1/2$ for parallel ($\theta = 0^\circ$) and perpendicular ($\theta = 90^\circ$) transitions, respectively.⁴⁹

III. RESULTS AND ANALYSIS

A. Photoelectron spectroscopy

Figure 3 shows the anion photoelectron spectra for CH_3OO^- and $C_2H_5OO^-$ at a detachment wavelength of 700 nm (1.771 eV). Franck-Condon simulations were performed using

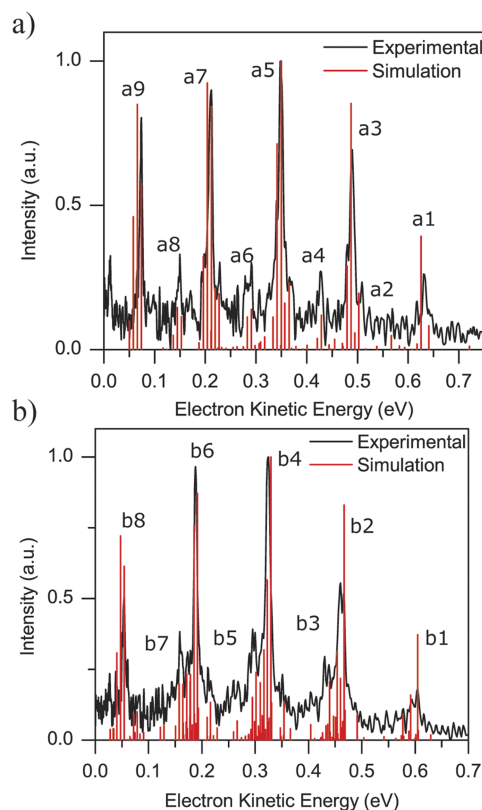


FIG. 3. Photoelectron spectra and Franck-Condon simulations of (a) CH_3OO^- and (b) $C_2H_5OO^-$ using a photon energy of 1.771 eV (700 nm). In the spectrum of $C_2H_5OO^-$, simulations of the gauche configuration are shown. Labels correspond to assignments made in Tables S1 and S2 in the [supplementary material](#).

EZSpectrum,⁵⁸ assuming an ion vibrational temperature of 300 K. Input vibrational frequencies and normal coordinates of both anion and neutral radicals were calculated using density functional theory with the B3LYP functional and 6-311G+(d,p) basis set using the Gaussian 09 package.⁵⁹ The calculated frequencies were scaled by a factor of 0.9679 as is appropriate for Pople style basis sets.⁶⁰

Both spectra in Fig. 3 exhibit a series of features becoming most intense in the middle of the spectrum, at $eKE \approx 0.30$ eV. Additionally, there are smaller, noisier peaks between those of the main progression. Simulations show that the major features of Fig. 3(a) correspond to progressions in the O–O stretch and the C–O–O bend with frequencies of 1112 cm^{-1} and 474 cm^{-1} , respectively. In the previously reported photoelectron spectrum of CH_3OO^- , the electron affinity of CH_3OO was determined to be 1.161 ± 0.005 eV, which is consistent with the location of the origin (labeled as a1) in Fig. 3(a).¹⁵ The main features were attributed to a progression in the O–O stretching mode (1124 cm^{-1}), and the smaller peaks were assigned as combination bands of the O–O stretch with the C–O–O bend (482 cm^{-1}), all of which are in reasonable agreement with our calculated values.¹⁵ Additionally, our assignments are consistent with those determined by Huang *et al.*¹² in which the O–O stretch was assigned to 1117 cm^{-1} . Similar vibrational assignments apply in Fig. 3(b), the spectrum for $\text{C}_2\text{H}_5\text{OO}^-$. The reported electron affinity of $\text{C}_2\text{H}_5\text{OO}$ is 1.186 ± 0.004 eV, which is consistent with the origin (labeled as b1) of Fig. 3(b).¹⁵ From our simulations and based on comparison with previous work, it is clear that the ion source is producing the desired species at a reasonably well-defined vibrational temperature. Assignments are tabulated in the [supplementary material](#) (Tables S1 and S2).

We generally seek to produce radicals in their ground vibrational state by photodetachment just above their electron affinity. One set of dissociation experiments of CH_3OO^- was performed at a detachment wavelength of 1064 nm (1.165 eV), where this condition is satisfied; the photoelectron spectrum at this wavelength comprises a single peak corresponding to the vibrational origin and can be found in the [supplementary material](#) (Fig. S2). The neutral $\text{C}_2\text{H}_5\text{OO}$ radical is not accessible via photodetachment using 1064 nm, so experiments were carried out on both radicals at a photodetachment wavelength of 700 nm, where the radical internal energy distribution is reflected in the photoelectron spectra shown in Fig. 3. Under these conditions, the internal energy distribution for both species peaks at 0.28 eV (corresponding to peaks a5 and b4, two quanta in the O–O stretch) and has a spread of about 0.6 eV.

B. Mass distributions

Figures 4(a) and 4(b) show the two-body and three-body mass distributions, respectively, for the dissociation of CH_3OO and CD_3OO . The two-body distribution for CH_3OO comprises two peaks centered at 16 and 31 Da. In the distribution for CD_3OO , shown in red, the peak at 16 Da does not significantly shift while the higher mass peak shifts to 34 Da. Products from mass channels 1A (O + CH_3O), 2A (O_2 + CH_3), and 3A (OH + CH_2O) are each separated by a single mass unit

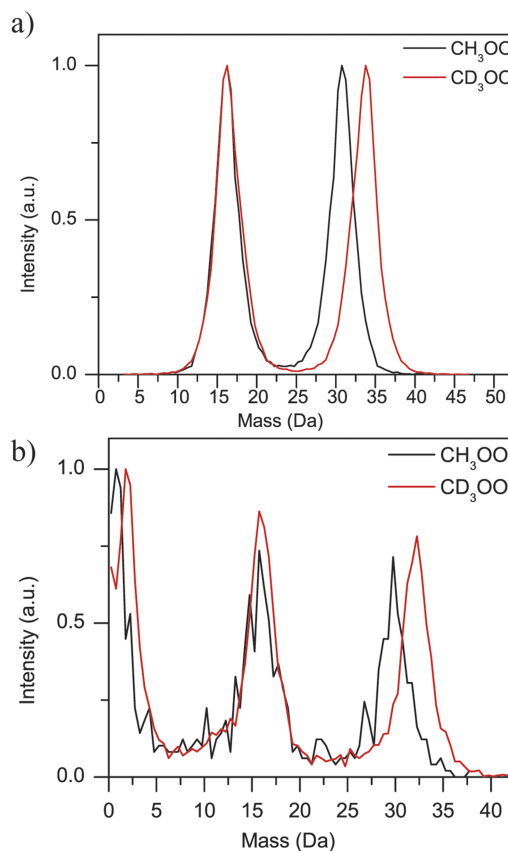


FIG. 4. (a) Two-body and (b) three-body photofragment mass distributions for CH_3OO (black) and CD_3OO (red) dissociation at 248 nm.

for the nondeuterated species, and the mass resolution of the experiment is insufficient to resolve contributions from these channels as distinct peaks. However, the peak locations for CH_3OO and the shifts observed upon deuteration indicate that channel 1A dominates. The presence of a small shift along the falling edge of the lower mass feature and the rising edge of the higher mass feature upon deuteration suggests the presence of 3A as a minor channel, an inference supported by simulations discussed in Sec. III D. The isotopic shifts and simulations rule out channel 2A.

In the three-body dissociation of CH_3OO [Fig. 4(b)], the mass distribution exhibits peaks at 1, 16, and 30 Da, and in the deuterated spectrum, the peaks occur at 2, 16, and 32 Da, identifying 4A (H + O + CH_2O) as the three-body channel. The spectra are quite noisy, particularly for CH_3OO ; this is due to the low number of detectable events resulting from the limitations of our experiment in detecting photofragment channels where H loss occurs.⁶¹ Due to the finite size of the detector and the presence of the beam block, two-body events with large fragment mass ratios, such as the production of H atoms and a heavier product, are generally undetectable in coincidence. In three-body dissociation, only the slowest H atoms impinge on the detector, and even these are not detected efficiently owing to their low kinetic energy in the laboratory frame-of-reference. Since D atoms are detected somewhat more efficiently than H atoms, the remaining data shown for channel 4A are from CD_3OO dissociation. Nonetheless, we do not expect that our results for channel 4A provide a holistic picture of the three-body dissociation mechanism as we are

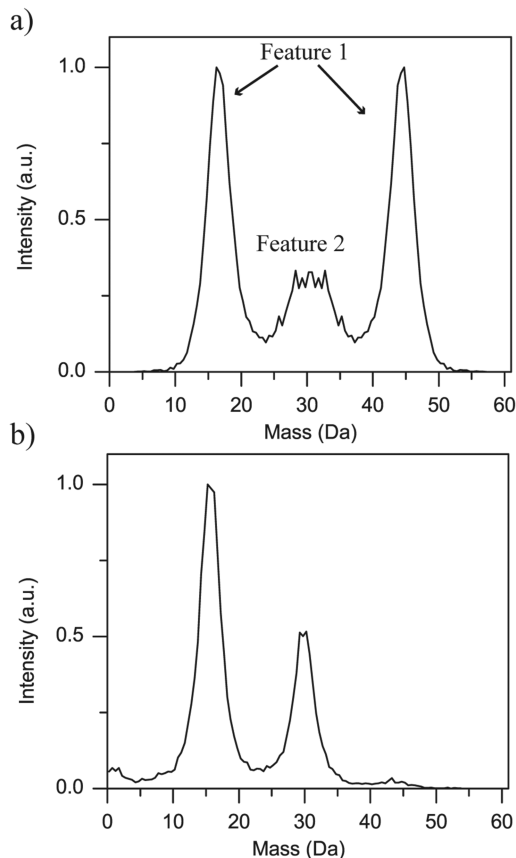


FIG. 5. Photofragment mass distributions for C_2H_5OO dissociation: (a) two-body mass distribution and (b) three-body mass distribution.

likely not detecting a significant number of true three-body events.

The two-body and three-body mass distributions for C_2H_5OO dissociation are shown in Figs. 5(a) and 5(b), respectively. The two-body mass distribution includes two distinct peaks (collectively referred to as Feature 1) centered about 16.5 and 44.5 Da that correspond to channels 1B ($O + C_2H_5O$) and either 6B ($OH + CH_3CHO$) or 7B ($OH + CH_2CH_2O$). Additionally, a smaller, broad distribution (Feature 2) ranges from 28 through 33 Da that can arise from channel 3B ($O_2 + C_2H_5$), channel 5B ($HO_2 + C_2H_4$), or some combination of the two.

The three-body mass distribution in Fig. 5(b) depicts two peaks at 15.5 Da and 30 Da. The peak at 15.5 Da is twice as intense as the peak at 30 Da, consistent with channel 4B ($CH_3 + O + CH_2O$).

C. Translational energy distributions and Dalitz plots

The translational energy of the products, E_T , is related to the endoergicity of a given process, ΔE_0 , the energy of the dissociation photon, $h\nu$, the internal energy of the reactants, E_{int}^R , and the internal energy of the products, E_{int}^P , through the following relationship:

$$E_T = h\nu - \Delta E_0 + E_{int}^R - E_{int}^P. \quad (2)$$

Typically, we seek to produce a fast beam of neutral radicals in their ground vibrational state by detaching anions at photon energies just above the electron affinity such that $E_{int}^R = 0$.

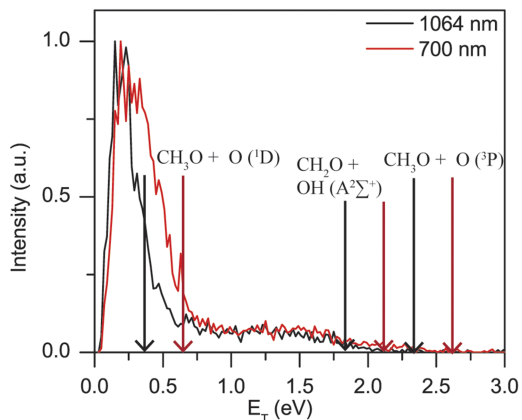


FIG. 6. Photofragment translational energy distribution for the two-body dissociation of CH_3OO radicals formed by photodetachment at 1064 nm (black) and 700 nm (red). Black and red arrows correspond to the maximum available translational energy for radicals dissociated using 1064 nm and 700 nm detachment wavelengths, respectively. The maximum available energy for the formation of channel 3A to form $CH_2O + OH(A^2\Sigma^+)$ is marked for both detachment wavelengths but the formation of $CH_2O + OH(X^2\Pi)$ exceeds 3.0 eV and is not marked.

As discussed in Sec. III A, higher photodetachment energies were also used; in those data sets, we take E_{int}^R as 0.28 eV and the spread in internal energy as 0.6 eV.

Figure 6 presents the two-body translational energy release for CH_3OO dissociation at both 700 nm and 1064 nm detachment wavelengths. This distribution is dominated by mass channel 1A and includes any events attributed to the minor dissociation channel 3A due to the insufficient mass resolution to distinguish product mass channels separated by 1 Da. The spectrum is bimodal with one very intense peak that tails off by 0.5 eV and 0.75 eV at 1064 and 700 nm, respectively, and a much smaller, broader feature extending out to about 2.0 eV. The lower translational energy feature in this distribution is anisotropic with $\beta = -0.60 \pm 0.10$ and $\beta = -0.68 \pm 0.11$ for 1064 nm and 700 nm detachment wavelengths, respectively, corresponding to a parallel transition for linearly polarized light. Angular information is unreliable for the higher energy release feature due to low signal.

At a dissociation energy of 5.00 eV (248 nm), mass channel 1A can comprise $CH_3O(X^2E)$ and atomic oxygen in either its ground 3P or excited 1D electronic state. For the formation of $CH_3O + O(^1D)$, the maximum available translational energy E_T^{max} is 0.36 eV for radicals in their ground vibrational state and 0.64 eV for radicals formed by electron detachment with 700 nm (ignoring the internal energy spread from photodetachment) as marked in Fig. 6. In going from a detachment wavelength of 1064 nm to 700 nm, the lower translational energy feature broadens considerably and cuts off around the corresponding value of E_T^{max} for $CH_3O + O(^1D)$ for both detachment wavelengths, so it is assigned to this channel. For the production of $CH_3O + O(^3P)$, the values of E_T^{max} are 2.32 eV and 2.60 eV for detachment wavelengths of 1064 nm and 700 nm, respectively. The high energy feature cuts off near these energies, suggesting at first glance that it should be assigned to $CH_3O + O(^3P)$. However, for any such fragments produced with $E_T < 1.42$ eV, the CH_3O fragment has enough energy to dissociate into $CH_2O + H$, leading to the three-body

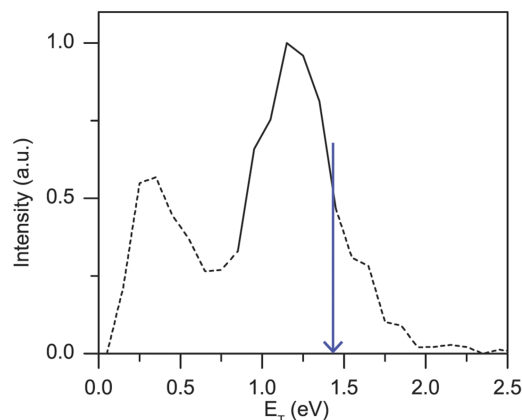


FIG. 7. Translational energy distribution for channel 4A using a detachment wavelength of 1064 nm. The blue arrow corresponds to the maximum available translational energy for this channel. The solid line presents the true peak of the distribution, while the dashed lines correspond to events attributed to false coincidences.

channel 4A discussed below. It is thus possible that some of the high energy feature below 1.42 eV is from OH loss (channel 3A), for which E_T^{\max} is 6.15 eV. The relative contributions of OH loss versus $O(^3P)$ loss to the distribution in the range $E_T > 1.42$ eV cannot be distinguished here. Note that for channel 3A, both $OH(X^2\Pi)$ or $OH(A^2\Sigma^+)$ are energetically accessible and E_T^{\max} is marked in in Fig. 6 only for the latter.

Figure 7 shows the DAF-corrected translational energy release for three body dissociation to $D + O(^3P) + CD_2O$ (channel 4A) from radicals formed using a detachment wavelength of 1064 nm. At first glance, the distribution appears bimodal, with one intense peak tailing off by 0.5 eV and a second broader feature extending to about 2.0 eV, above E_T^{\max} for this channel (1.42 eV). However, this spectrum is contaminated by false coincidences. Only the solid line shown in Fig. 7 is representative of the true distribution, as explained in the following analysis.

The number of detected three-body dissociation events is significantly smaller than that of two-body events such that

there is a greater chance of the three-body dissociation data to be contaminated by false coincident events, in which a third particle is accepted within the same laser shot as two true fragments. As such, simulations were performed to accept two-body events with some probability of detecting a third fragment with a random arrival position and time within the constraints of the detector. Generated fragment coordinates were analyzed to produce mass distributions and translational energy distributions. The resulting simulated translational energy distribution for CD_3OO dissociation (shown in Fig. S3 of the [supplementary material](#)) exhibits a strong feature with low translational energy release and extends well beyond E_T^{\max} for channel 4A formation. Hence, both the low energy peak and signal beyond E_T^{\max} are attributed to false coincidences, and only the major feature at high translational energy release is attributed to true dissociation events from channel 4A. This feature extends to E_T^{\max} for $CH_3 + O(^3P) + CH_2O$ formation; $O(^1D)$ is not accessible via three-body dissociation. For $E_T \geq 0.80$ eV, the angular distribution is anisotropic with $\beta = 0.44 \pm 0.06$, consistent with the three-body dissociation plane tending to lie parallel to the plane of laser polarization.

Figure 8 presents the two-body translational energy distributions for C_2H_5OO dissociation experiments performed using a detachment wavelength of 700 nm. The translational energy distribution for Feature 1 of the mass distribution (O and OH loss) is shown in Fig. 8(a). The distribution tails off by 0.5 eV with a very sharp peak close to 0 eV and extends with some intensity out to 2.0 eV. E_T^{\max} for dissociation to form $O(^1D) + CH_3CH_2O$, when taking into account internal energy, is 0.57 eV and is 2.53 eV for the formation of $O(^3P) + CH_3CH_2O$. Similar to the distributions presented for CH_3OO dissociation, the narrow peak at low translational energy is assigned to the formation of $CH_3CH_2O + O(^1D)$, while dissociation events leading to $CH_3CH_2O + O(^3P)$ production may result in further fragmentation for photoproducts with less than 2.02 eV of translational energy. For dissociation via $OH(X^2\Pi)$ loss, E_T^{\max} for channels 6B and 7B is 6.31 eV and 5.14 eV, respectively. $OH(A^2\Sigma^+)$ loss can also from channel 6B

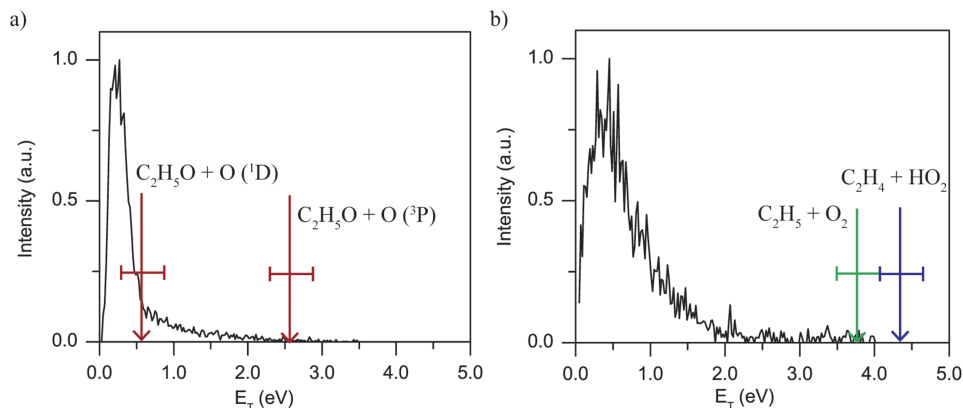


FIG. 8. Photofragment translational energy distribution for C_2H_5OO dissociation to (a) Feature 1 (channel 1B and channel 6B/7B). The red arrows depict the maximum available energy for O loss. The horizontal bar depicts the range of internal energy that the radicals may contain. Channels 6B and 7B both result in OH loss, but the maximum available energies for both channels are greater than 5.0 eV and are not marked on the spectrum. (b) Dissociation to Feature 2 (channel 3B and 5B). The green and blue arrows mark the maximum available energy for O_2 loss and HO_2 loss, respectively. The associated horizontal bars depict the range of internal energy within the dissociating radicals.

or 7B, for which E_T^{\max} is 2.26 eV and 1.09 eV, respectively. The angular distribution is anisotropic in the low translational energy region with $\beta = -0.56 \pm 0.08$, corresponding to a parallel transition for linear laser polarization.

Figure 8(b) shows the translational energy release for Feature 2 of the mass distribution (O_2 and HO_2 loss). The values of E_T^{\max} for channel 3B and channel 5B are 3.74 eV and 4.31 eV, respectively. Figure 8(b) depicts a single feature peaking around 0.5 eV that tails off by about 2.0 eV with some observable intensity extending to 4.0 eV. The angular distribution is isotropic.

The translational energy distribution for the three-body channel 4B is shown in Fig. 9(a). The distribution appears to be bimodal with one feature peaking just below 0.5 eV and tailing off around 0.75 eV and a second, broader feature that peaks around 1.5 eV and extends to 2.5 eV. E_T^{\max} for this channel is 2.02 eV. Similar to CD_3OO dissociation, simulations (Fig. S4 of the supplementary material) demonstrate that the lower energy peak is due to false coincidences, but in contrast to CD_3OO , false coincidences do not extend to higher E_T . The higher energy feature extends to E_T^{\max} for experiments performed using a detachment wavelength of 700 nm, and its angular distribution yields $\beta = 0.22 \pm 0.04$. We note that $\beta > 0$ for the three-body dissociation of CD_3OO , C_2H_5OO , and t -BuOO, indicating that for all three peroxy radicals, the dissociation plane tends to lie parallel to the laser polarization plane, although this description is misworded in the t -BuOO study by Nichols *et al.*⁵

Figure 9(b) shows a Dalitz plot for channel 4B. These plots are useful in understanding the energy and momentum partitioning amongst the three photofragments as well as the dissociation mechanism. All dissociation events are restricted to lying within the triangle by conservation of energy with the colored arrows representing the fraction of energy, ε_i , partitioned in a given fragment where $0 \leq \varepsilon_i \leq 1$. Conservation of momentum requires that all physically meaningful events lie within the inscribed ellipse. Each point on the Dalitz plot provides information about the momentum and energy partitioning to each of the three fragments. Although a Dalitz plot was obtained for CD_3OO dissociation to channel 4A (Fig. S5

of the supplementary material), it provides only a partial view of the three-body dissociation since only the slowest D atoms were detected and is thus much less informative than the plots in Fig. 9.

The Dalitz plot for channel 4B exhibits two broad regions of intensity originating at the base of the blue arrow, corresponding to very little energy in the CH_2O fragment, extending to the bases of the green and red arrows, where there is small partitioning of energy in the O atom and CH_3 fragment, respectively. The spots of greatest intensity are at the base of each of the three arrows. For the entire distribution, the average partitioning in each fragment is $\langle \varepsilon_{CH_3} \rangle = 0.35$, $\langle \varepsilon_O \rangle = 0.38$, and $\langle \varepsilon_{CH_2O} \rangle = 0.27$. The photoproducts O and CH_3 , which are almost identical in mass, cannot be sufficiently distinguished from one another in the analysis so that the partitioning of momentum amongst the two is not accurately depicted. Thus, the plot in Fig. 9(b) is symmetric about the blue line. Based on the discussion in Sec. IV, events in which the O atoms are slow, i.e., those near the base of the green arrow, are likely to be improperly assigned. Therefore, one obtains a clearer picture of the true Dalitz plot by “folding over” the blue arrow, as shown in Fig. 9(c).

D. Branching ratios

One goal of this experiment is to determine branching ratios of the photofragment channels. To distinguish between two- and three-body dissociation channels, the raw number of events in each was used to determine the two- to three-body branching ratio. For channel 4B from C_2H_5OO , this ratio was corrected for the lower detection probability of three fragments as opposed to two in the following way: the given detection probability of a single event on the detector is $p_{\text{particle}} = 0.6$, so the probability of detecting all fragments from a dissociation event is $p_{\text{two-body}} = 0.36$ and $p_{\text{three-body}} = 0.22$.⁶² However, for CH_3OO dissociation to channel 4A, the detection efficiency for D atoms is significantly lower than 0.6, and thus, the overall three-body event detection probability is even smaller in this case. Previous studies performed in our laboratory have found the detection probability of D atoms to be about 0.08, and

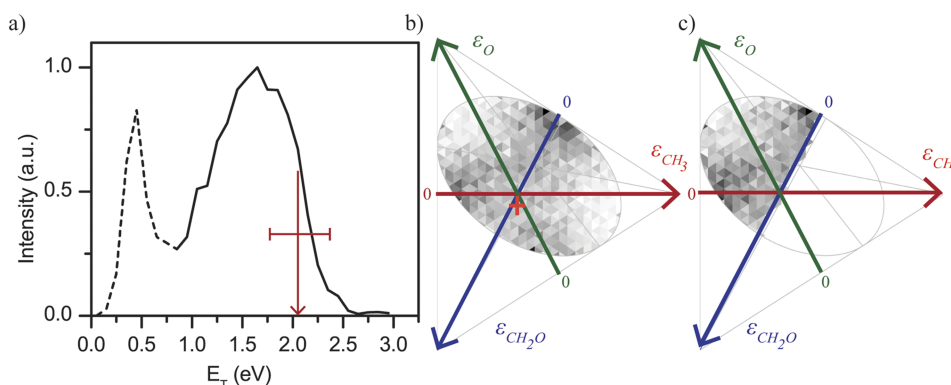


FIG. 9. (a) Photofragment translational energy distribution for C_2H_5OO dissociation to channel 4B. The solid line shows the true distribution, while the dashed portion is attributed to false coincidences. The red arrow marks the maximum available energy, and the associated horizontal bar marks the range of internal energy of the radicals. (b) Dalitz plot for the three-body dissociation of C_2H_5OO to channel 4B plotted for the high energy feature of the translational energy distribution. The orange cross marks the calculated position for the synchronous concerted dissociation of C_2H_5OO . (c) Dalitz plot from (b), folded over such that events in which the slow O atoms are improperly assigned (see text) are reflected across the blue line to more accurately depict the true Dalitz plot.

TABLE I. Product yields for CD₃OO and C₂H₅OO photodissociation.

| Product channel | Percentage of total events |
|---|----------------------------|
| CD ₃ OO → 1A (O loss) | 55 ± 5 |
| CD ₃ OO → 3A (OD loss) | 6 ± 3 |
| CD ₃ OO → 4A (D + O + CD ₂ O) | 39 ± 5 |
| C ₂ H ₅ OO → 1B (O loss) | 29 ± 4 |
| C ₂ H ₅ OO → 6B/7B (OH loss) | 22 ± 3 |
| C ₂ H ₅ OO → 3B (O ₂ loss) | 4 ± 2 |
| C ₂ H ₅ OO → 5B (HO ₂ loss) | 3 ± 1 |
| C ₂ H ₅ OO → 4B (CH ₃ + O + CH ₂ O) | 42 ± 3 |

we thus use $p_{\text{three-body}} = 0.0288$ to determine the channel 4A product yield.^{61,63}

Table I presents the branching ratios for photofragment production for both radicals (using CD₃OO instead of CH₃OO). For the two-body dissociation of both CD₃OO and C₂H₅OO, the two-body mass distributions were simulated to a best fit using the corresponding translational energy distribution. The mass resolution of the spectrometer is $m/\Delta m \approx 10$,⁶⁴ so two-body mass channels in which fragments differ by 1 Da (1A and 3A, for example) cannot be cleanly resolved. In such cases, photofragment branching ratios were determined by fitting the mass distributions in Figs. 4(a) and 5(a), assuming the same translational energy distribution for each pair of channels differing by 1 Da, i.e., the distributions in Fig. 6 (for channels 1A and 3A), Fig. 8(a) (for channels 1B and 6B/7B), and Fig. 8(b) (for channels 3B and 5B).

The reported errors represent the standard deviation of the branching ratios determined for all data sets of given detachment and dissociation energy and do not account for other assumptions made (such as detection probability corrections); i.e., they are random, not systematic, error bars. The simulated spectra are presented in comparison with the experimental data in the [supplementary material](#); see Figs. S6–S8. As explained previously, we only observe a small fraction of the dissociation events for the three-body dissociation of CD₃OO due to constraints of the detector size that we attempt to compensate for with the assumed value of $p_{\text{three-body}}$, as discussed above. Therefore, the reported contribution from channel 4A is expected to have a large systematic error. However, the 1A:3A branching ratio of 9.2:1 inferred from Table I is independent of the channel 4A contribution. Hence, we can say that O(¹D) production is the dominant two-body dissociation channel for CD₃OO, and that this channel is significant but considerably less dominant for C₂H₅OO.

IV. DISCUSSION

A. CH₃OO two-body dissociation

This experiment seeks to determine what products are formed in the dissociation of the alkyl peroxy radicals and the mechanism by which dissociation occurs. To do so, we examine the translational energy and angular distributions of each product channel more closely.

The translational energy distribution in Fig. 6 for channels 1A (O + CH₃O) and 3A (OH + CH₂O) consists of two distinct

features: one intense feature peaking very close to zero and tailing off before 1.0 eV and a much less intense, broader feature extending out to 2.0 eV. In Sec. III C, the feature at low E_T was assigned to O(¹D) + CH₃O. The benefit of performing experiments at two different detachment energies manifests itself in noting that this feature broadens considerably upon increasing the detachment energy from 1.165 eV (1064 nm) to 1.771 eV (700 nm). As the extra 0.28 eV of vibrational energy in the radical from photodetachment at 700 nm is localized almost exclusively in the O–O stretch, and the peak extends to E_T^{max} at both wavelengths, this distribution is consistent with dissociation along a repulsive surface to form O(¹D) + CH₃O. Further evidence supporting direct dissociation is the anisotropic angular distribution for the low E_T peak, which indicates a parallel electronic transition and dissociation considerably faster than a rotational period.

To aid in understanding these results, we look to an analogous system: HO₂. In the 220-nm photolysis of HO₂, O(¹D) + OH were observed as the dominant photofragments, similar to what is seen here in CH₃OO, with O(³P) accounting for only 16% of the product yield.²² Vazquez *et al.*⁶⁵ investigated the electronic surfaces of HO₂ and determined that the \tilde{B}^2A'' state is the only Franck-Condon accessible state with reasonable oscillator strength for a transition from the ground state in the region of 220 nm, where the UV absorption spectrum of HO₂ has a maximum.¹ This state diabatically correlates to O(¹D) + OH products and, as the O–O bond stretches, intersects other potential energy curves that lead to O(³P) formation. Experimentally, the O(¹D) + OH products dominate,²² so it would appear that the dissociation is diabatic and that the curve crossings are inefficient. Such a scenario is a signature of rapid, repulsive dissociation on the \tilde{B}^2A'' state.

Similar computational work examining CH₃OO has been performed by Jafri and Phillips⁸ in which the O–O bond has been shown to be repulsive in the Franck-Condon accessible region of several excited states, but the authors do not address the likelihood of forming the two electronic states of atomic oxygen. However, generalized valence bond diagrams for peroxy radicals in the \tilde{B}^2A'' state show that the cleavage of the O–O bond correlates with O(¹D) formation,^{15,66,67} suggesting that the CH₃OO excited state surface mimics that of HO₂. This, in combination with the parallel angular distribution observed in our experiment, is consistent with an electronic transition to the \tilde{B}^2A'' state to yield O(¹D) + CH₃O products with small amounts of curve crossing leading to O(³P) formation.

With evidence supporting the claim that the dominant product channel, CH₃O + O(¹D), forms through excited state dissociation, the remaining question of interest is whether any product channels are formed via internal conversion to the ground state followed by statistical dissociation. According to Fig. 1, channel 2A (O₂ + CH₃) is the most energetically accessible channel on the ground state surface. While several other channels are asymptotically lower in energy than channel 2A, they require isomerization over sizeable barriers, whereas simple C–O bond fission to form channel 2A necessitates the least amount of energy. Statistical dissociation following internal conversion to the ground electronic state would therefore lead to channel 2A as a competitive product channel. Since this channel is not observed here, the remaining dissociation

channels to be considered likely do not form through a statistical decay dissociation mechanism on the ground electronic state.

The higher-energy, weaker feature in Fig. 6 extends to about 2.3 eV, just below E_T^{\max} for the $O(^3P)$ loss channel. Any $CH_3O + O(^3P)$ formed with $E_T < 1.42$ eV has enough internal energy to further dissociate, which suggests that much of the weaker feature below this energy is from OH loss. The distribution extends well beyond 1.42 eV, however, and any $CH_3O + O(^3P)$ in this energy region cannot undergo further fragmentation. Hence, we attribute the weaker feature to a combination of $OH + CH_2O$ and $O(^3P) + CH_3O$, with both processes most likely occurring on an excited state surface based on the above discussion.

In previous work by Hartmann *et al.*²⁰ on the photodissociation of CH_3OO at 248 nm, both $OH(X^2\Pi)$ and $OH(A^2\Sigma^+)$ were identified by laser-induced fluorescence and emission spectroscopy. They proposed isomerization to QOOH on the excited state surface as the source of $OH(A^2\Sigma^+)$. The value of E_T^{\max} for the formation of $CH_2O + OH(A^2\Sigma^+)$ is 2.10 eV, which is about where the smaller feature in Fig. 6 loses intensity. However, we cannot, at present, identify the electronic state of OH produced without an understanding of the possible pathways beyond the ground electronic state surface.

Hartmann *et al.* reported a branching ratio of O loss: OH loss of $77\% \pm 39\%$: $23\% \pm 12\%$ and, through mass balance, concluded that $O_2 + CH_3$ is the dominant channel, comprising $74\% \pm 13\%$ of the photoproducts.²⁰ While the O:OH branching ratio is in fair agreement with that determined in this work, $55\% \pm 6\%$: $6\% \pm 3\%$ (with the remaining 39% attributed to channel 4A), we see no evidence of $O_2 + CH_3$. As Hartmann *et al.* used laser induced fluorescence and emission spectroscopy to detect one fragment of dissociation product channels, they would not have the capability to identify a three-body channel. Our reported branching ratio for channel 4A production (39%) may account for a significant portion of the unseen photoproduct yield inferred by Hartmann *et al.*

B. C_2H_5OO two-body dissociation

We next consider the two-body dissociation of C_2H_5OO . Figure 8(a) shows the translational energy distribution for the events corresponding to Feature 1 in the mass distribution of Fig. 5(a). The sharp peak at low E_T drops substantially in intensity by 0.5 eV, and the photofragment angular distribution is anisotropic over the energy range covered by this peak. As in CH_3OO dissociation, the photon energy used in this experiment is sufficient such that both $C_2H_5O(\tilde{X}^2A'') + O(^1D)$ and $C_2H_5O(\tilde{X}^2A'') + O(^3P)$ can be formed with E_T^{\max} of 0.57 eV and 2.53 eV, respectively. The formation of $C_2H_5O(\tilde{X}^2A'') + O(^1D)$ on a repulsive surface is consistent with the translational and anisotropic angular distributions associated with the low energy peak. The negative anisotropy parameter ($\beta = -0.56$) associated with this low energy feature suggests a parallel transition to the \tilde{B}^2A'' state which, as discussed in Sec. IV A, leads predominantly to the formation of $O(^1D)$ with the possibility of curve crossing to produce $O(^3P)$. When this occurs, any $C_2H_5O + O(^3P)$ products with less than 2.02 eV of translational energy can dissociate further (channel 4B, for

example) and should not contribute to the two-body signal. For this reason, the high translational energy release tail in Fig. 8(a) is mostly attributed to OH loss, although OH loss contributes to the intense feature at low E_T as well.

The potential energy surface in Fig. 2 shows multiple low lying dissociative pathways on the ground electronic state, the most facile of which lead to channels 3B ($O_2 + C_2H_5$) or 5B ($HO_2 + C_2H_4$), both of which can contribute to Feature 2 in Fig. 5. On the ground state, channel 3B formation through barrierless C–O bond cleavage would impart very little translational energy in the products. Channel 5B can occur through either a direct process, in which dissociation occurs over a barrier, or an indirect process, in which a highly internally excited C_2H_5OO isomerizes to form the QOOH species followed by dissociation after overcoming a second barrier. In this instance, for direct and indirect HO_2 losses, the barriers with respect to the products are 0.35 eV and 0.49 eV, respectively. In examining the translational energy distribution for channels 3B and 5B, there is one main, broad feature peaking around 0.5 eV, consistent with both O_2 and HO_2 losses occurring on the ground electronic state.

We can calculate product branching ratios for ground state dissociation using Rice–Ramsperger–Kassel–Marcus (RRKM) theory,⁶⁸ in which the microcanonical dissociation rate constant $k(E)$ is given by

$$k(E) = \frac{W^\ddagger(E - E_0)}{h\rho(E)}, \quad (3)$$

where $W^\ddagger(E - E_0)$ is the sum of states of the transition state, $\rho(E)$ is the density of states of the reactant, and h is Planck's constant. The vibrational sum and density of states were calculated using the Beyer-Swinehart algorithm.⁶⁹ Further details are presented in the [supplementary material](#).

Table II shows the rate constants for each of these processes. The RRKM calculations show that channel 5B occurs primarily by the direct pathway rather than by isomerization to QOOH. This is as one might expect, given that the direct pathway is lower in energy. In addition, the RRKM calculations yield a branching ratio of O_2 : HO_2 loss of 3.42:1, reasonably close to the ratio from Table I of 1.33:1 that was obtained by simulating the mass distributions. This agreement, along with the general appearance of the product translational energy distribution, suggests that channels 3B and 5B are the result of statistical dissociation on the ground state. A similar mechanism was proposed for the analogous channels in the photodissociation of the *t*-BuOO radical.⁵

The RRKM calculations also show that the rate of formation of OH on the ground state, either directly or indirectly, is an order of magnitude smaller than that for HO_2 and O_2 loss.

TABLE II. RRKM rate constants for C_2H_5OO dissociation.

| Pathway | Rate (s^{-1}) |
|-----------------------|-----------------------|
| Channel 5B (direct) | 2.98×10^{11} |
| Channel 5B (indirect) | 1.42×10^{10} |
| Channel 3B | 1.02×10^{12} |
| Channel 6B | 9.22×10^{10} |
| Channel 7B | 3.34×10^{10} |

Since more rather than less OH is formed relative to these two channels, according to Table I, OH loss to produce channel 6B (OH + CH₃CHO) or 7B (OH + CH₂CH₂O) likely occurs on an excited state. The translational energy distribution in Fig. 8(a) peaks below E_T^{\max} for the formation of both OH electronic states for each channel, but further understanding of which channel is formed cannot be known from our study.

C. CD₃OO and C₂H₅OO three-body dissociation

The three-body dissociation of CD₃OO and C₂H₅OO is discussed together as they exhibit similar dynamics. The portion of the translational energy distribution for CD₃OO dissociation to channel 4A (D + O(³P) + CD₂O) that is attributed to true three-body events extends to E_T^{\max} [Fig. 7(a)], indicating that this process involves, in some way, a dissociative surface. As discussed previously,^{5,22} the O–O bond in peroxy radicals is repulsive on the \tilde{B}^2A'' state surface accessed near 248 nm and, through curve crossing, can lead to the production of O(³P). For C₂H₅OO dissociation to channel 4B (O(³P) + CH₃ + CH₂O), the true three-body translational energy distribution (the higher energy peak) in Fig. 9(a) also extends up to E_T^{\max} . Moreover, the photofragment angular distributions associated with the translational energy distributions for both CD₃OO and C₂H₅OO are anisotropic with positive β values that indicate that the dissociation plane tends to lie parallel to the plane of laser polarization, consistent with a parallel electronic transition to the \tilde{B}^2A'' state for both species. Thus, we propose that channels 4A and 4B are produced through excitation to the \tilde{B}^2A'' state followed by curve crossing to a repulsive surface with respect to the O–O bond length to yield O(³P) and the relevant alkoxy fragment (CD₃O and C₂H₅O, respectively). Then, provided it has sufficient internal energy, the alkoxy radical dissociates to the respective products.

Three-body dissociation processes can be further investigated by classifying the dissociation mechanism according to the time scale and assigning one of two definitions: concerted and sequential.⁷⁰ Sequential dissociation events are defined as events in which the molecule of interest dissociates into two fragments, and a substantial quantity of time (longer than a rotational period) passes before the second dissociation event occurs. Concerted dissociation events are typically characterized by an equal partitioning of momentum in the two leaving products and can be distinguished further as either synchronous or asynchronous. Synchronous concerted dissociation events result in three fragments formed simultaneously, on a time scale much less than a rotational period, while asynchronous concerted dissociation events occur on a non-zero time scale less than or comparable to a rotational period. In the discussion of both CH₃OO and C₂H₅OO, the O atom is proposed to depart first with substantial translational energy, followed by the subsequent dissociation of the remaining alkoxy fragment, thereby eliminating synchronous concerted dissociation as a possibility.

Dalitz plots provide further insights into the three-body dissociation mechanism. Here, such a plot is available only for C₂H₅OO on which our focus will remain. In the proposed mechanism, the departing O atom is fast, and the subsequent dissociation of the energized C₂H₅O to CH₃ + CH₂O should

produce relatively slow fragments. This is the justification for “folding” the Dalitz plot in Fig. 9(b) to produce the plot in Fig. 9(c); Fig. 9(b) has significant intensity at the base of the green arrow that most likely represents slow CH₃ fragments that were incorrectly assigned as slow O fragments. The most intense regions of the folded plot are at the base of the blue and red arrows corresponding to slow CH₂O and CH₃, respectively, which is consistent with the idea that the O atom leaves first repulsively with a substantial fraction of translational energy and indicates that Fig. 9(c) is a more accurate representation of the three-body dynamics.

Such a plot can help distinguish sequential from asynchronous concerted dissociation. While either mechanism would manifest as a pattern of slow CH₂O and CH₃ in the Dalitz plot, sequential dissociation would result in a well-defined stripe across the green arrow, corresponding to a relatively constant fraction of the energy imparted to the O atom as seen previously in the photodissociation of diiodobromide (I₂Br⁻)⁷¹ or in the fragmentation of CO₂³⁺ via collisions with slow highly charged ions.⁷² Though there is a broad swath across the green arrow, it lacks a defined structure consistent with the sequential dissociation of the aforementioned triatomic systems, although a broader feature would be expected for polyatomic systems such as C₂H₅OO. However, the anisotropic angular distribution observed for C₂H₅OO three-body dissociation is indicative of the ethoxy dissociation occurring on the order of a rotational period as its persistence for several rotational periods (characteristic of a sequential mechanism) would likely yield an isotropic distribution. Hence, an asynchronous concerted mechanism is the most appropriate classification.

These dynamics are of interest in light of our recent study on the *t*-BuOO radical for which the dominant dissociation channel was O(³P) + CH₃ + (CH₃)₂CO formed via repulsive O loss. In comparing C₂H₅OO and *t*-BuOO, the barrier for *t*-butoxy dissociation to acetone and CH₃ is 0.55 eV,⁷³ less than that for ethoxy. More interestingly, *t*-BuOO dissociation did not yield any O(¹D) loss, the dominant two-body channel for CH₃OO and C₂H₅OO. We have claimed here that both two- and three-body processes originate via the same electronic transition, but interactions between the excited state surfaces are required to produce O(³P) and thus, three-body products. As mentioned above, studies examining the excited states of HO₂ suggest this curve crossing from the \tilde{B} state to form O(³P) occurs infrequently due to weak interactions of the relevant surfaces. It is evident, however, that for C₂H₅OO and *t*-BuOO, the three-body O(³P) production becomes a more competitive process for the larger alkyl substituents, and thus O(¹D) production is less frequent. This trend suggests that there are more favorable interactions allowing for curve crossing from the \tilde{B} state to occur in these larger radicals, as would be logical for more degrees of freedom, thereby suppressing O(¹D) formation. Additionally, the endoergicity for O(¹D) production rises with increasing alkyl group size and is 4.81 eV for *t*-BuOO,^{74,75} compared to 4.71 eV for C₂H₅OO and 4.64 eV for CH₃OO. It is possible that this repulsive state is accessed in all three radicals, but the higher endoergicity for O(¹D) production from *t*-BuOO leads to slower dissociation dynamics on this state, allowing for the other channels to dominate

via conical intersections or other non-adiabatic decay mechanisms. Finally, we note that two-body dissociation via internal conversion to the ground state followed by statistical decay to O₂ and HO₂ products becomes more prominent in progressing from CH₃OO, where no evidence for this process is seen, to *t*-BuOO, where it is the sole two-body channel. Hence, the non-adiabatic interactions leading to ground state population become more prominent as the size of the alkyl substituent increases.

V. CONCLUSIONS

Photofragment translational spectroscopy was used to investigate the unimolecular dissociation dynamics of the simplest alkyl peroxy radicals, CH₃OO and C₂H₅OO. Both radicals exhibit two-body dissociation to O(¹D) via direct dissociation on a repulsive excited state. Each radical dissociates to a three-body channel for which the translational energy distributions peak near the maximum available energy for the process. The mechanism is attributed to repulsive O loss followed by the dissociation of the respective alkoxy fragment. In addition, C₂H₅OO exhibits significant OH loss, comparable in quantity to O loss. Additionally, O₂ and HO₂ losses from C₂H₅OO contribute and are attributed to statistical decay on the ground state surface. C₂H₅OO photoexcitation results in the formation of product channels consistent with both a smaller alkyl peroxy (CH₃OO) and a larger one (*t*-BuOO). Thus, as the alkyl substituent increases in size, statistical decay on the ground state becomes a more competitive process, while the excited state O(¹D) production becomes less prevalent.

SUPPLEMENTARY MATERIAL

See [supplementary material](#) for NMR spectrum, photoelectron assignments, simulations of two- and three-body events, and details of RRKM calculations.

ACKNOWLEDGMENTS

The authors would like to thank Cynthia Hong for her discussions of the chemical syntheses of alkyl hydroperoxides. The authors would also like to thank Joonho Lee and Luke Bertels for assistance with some theoretical work. This research was supported by the Director, Office of Basic Energy Science, Chemical Sciences Division of the U.S. Department of Energy under Contract No. DE-AC02-05CH11231.

¹P. D. Lightfoot, R. A. Cox, J. N. Crowley, M. Destriau, G. D. Hayman, M. E. Jenkin, G. K. Moortgat, and F. Zabel, *Atmos. Environ. A* **26**, 1805 (1992).

²J. Zádor, C. A. Taatjes, and R. X. Fernandes, *Prog. Energy Combust. Sci.* **37**, 371 (2011).

³G. S. Tyndall, R. A. Cox, C. Granier, R. Lesclaux, G. K. Moortgat, M. J. Pilling, A. R. Ravishankara, and T. J. Wallington, *J. Geophys. Res.* **106**, 12157, <https://doi.org/10.1029/2000jd900746> (2001).

⁴E. W. Kaiser, *J. Phys. Chem.* **99**, 707 (1995).

⁵B. Nichols, E. N. Sullivan, M. Ryazanov, C. Hong, and D. M. Neumark, *J. Chem. Phys.* **147**, 134304 (2017).

⁶C. J. Hochandel, J. A. Ghormley, J. W. Boyle, and P. J. Ogren, *J. Phys. Chem.* **81**, 3 (1977).

⁷C. Anastasi, I. W. M. Smith, and D. A. Parkes, *J. Chem. Soc., Faraday Trans. 1* **74**, 1693 (1978).

⁸J. A. Jafri and D. H. Phillips, *J. Am. Chem. Soc.* **112**, 2586 (1990).

⁹T. J. Wallington, P. Dagaut, and M. J. Kurylo, *Chem. Rev.* **92**, 667 (1992).

¹⁰G. Chettur and A. Snelson, *J. Phys. Chem.* **91**, 3483 (1987).

¹¹P. Ase, W. Bock, and A. Snelson, *J. Phys. Chem.* **90**, 2099 (1986).

¹²D.-R. Huang, L.-K. Chu, and Y.-P. Lee, *J. Chem. Phys.* **127**, 234318 (2007).

¹³K.-H. Hsu, Y.-H. Huang, Y.-P. Lee, M. Huang, T. A. Miller, and A. B. McCoy, *J. Phys. Chem. A* **120**, 4827 (2016).

¹⁴M. Huang, T. A. Miller, A. B. McCoy, K.-H. Hsu, Y.-H. Huang, and Y.-P. Lee, *J. Phys. Chem. A* **121**, 9619 (2017).

¹⁵S. J. Blanksby, T. M. Ramond, G. E. Davico, M. R. Nimlos, S. Kato, V. M. Bierbaum, W. C. Lineberger, G. B. Ellison, and M. Okumura, *J. Am. Chem. Soc.* **123**, 9585 (2001).

¹⁶M. B. Pushkarsky, S. J. Zalyubovsky, and T. A. Miller, *J. Chem. Phys.* **112**, 10695 (2000).

¹⁷P. Rupper, E. N. Sharp, G. Tarczay, and T. A. Miller, *J. Phys. Chem. A* **111**, 832 (2007).

¹⁸G. M. P. Just, P. Rupper, T. A. Miller, and W. L. Meerts, *J. Chem. Phys.* **131**, 184303 (2009).

¹⁹G. Meloni, P. Zou, S. J. Klippenstein, M. Ahmed, S. R. Leone, C. A. Taatjes, and D. L. Osborn, *J. Am. Chem. Soc.* **128**, 13559 (2006).

²⁰D. Hartmann, J. Kärthäuser, and R. Zellner, *J. Phys. Chem.* **94**, 2966 (1990).

²¹C. Kassner, P. Heinrich, F. Stuhl, S. Couris, and S. Haritakis, *Chem. Phys. Lett.* **208**, 27 (1993).

²²M. Lock, R. Barnes, and A. Sinha, *J. Chem. Phys.* **104**, 1350 (1996).

²³B. Ruscic and D. H. Bross, Active Thermochemical Tables (ATcT) values based on version 1.122 of the Thermochemical Network, available at ATcT.anl.gov, 2016.

²⁴S. Saebo, L. Radom, and H. F. Schaefer III, *J. Chem. Phys.* **78**, 845 (1983).

²⁵S. P. Walch, *Chem. Phys. Lett.* **215**, 81 (1993).

²⁶Y.-S. Cheung and W.-K. Li, *Chem. Phys. Lett.* **223**, 383 (1994).

²⁷W. H. Green, *Int. J. Quantum Chem.* **52**, 837 (1994).

²⁸E. Sicilia, F. P. D. Maio, and N. Russo, *Chem. Phys. Lett.* **225**, 208–212 (1994).

²⁹Y.-S. Cheung and W.-K. Li, *J. Mol. Struct.: THEOCHEM* **333**, 135 (1995).

³⁰R. Zhu, C.-C. Hsu, and M. C. Lin, *J. Chem. Phys.* **115**, 195 (2001).

³¹A. Stoebner and R. Delbourgo, *J. Chim. Phys.* **64**, 1115 (1967).

³²J. W. Bozzelli and A. M. Dean, *J. Phys. Chem.* **94**, 3313 (1990).

³³A. F. Wagner, I. R. Slagle, D. Sarzynski, and D. Gutman, *J. Phys. Chem.* **94**, 1853 (1990).

³⁴G. E. Quench, M. M. Gallo, and H. F. Schaefer III, *J. Am. Chem. Soc.* **114**, 8239 (1992).

³⁵G. E. Quench, M. M. Gallo, M. Shen, Y. Xie, H. F. Schaefer III, and D. Moncrieff, *J. Am. Chem. Soc.* **116**, 4953 (1994).

³⁶I. S. Ignatyev, Y. Xie, W. D. Allen, and H. F. Schaefer III, *J. Chem. Phys.* **107**, 141 (1997).

³⁷J. C. Rienstra-Kiracofe, W. D. Allen, and H. F. Schaefer III, *J. Phys. Chem. A* **104**, 9823 (2000).

³⁸J. A. Miller, S. J. Klippenstein, and S. H. Robertson, *Proc. Combust. Inst.* **28**, 1479 (2000).

³⁹M. S. Stark, *J. Am. Chem. Soc.* **122**, 4162 (2000).

⁴⁰J. A. Miller and S. J. Klippenstein, *Int. J. Chem. Kinet.* **33**, 654 (2001).

⁴¹C. Y. Sheng, J. W. Bozzelli, A. M. Dean, and A. Y. Chang, *J. Phys. Chem. A* **106**, 7276 (2002).

⁴²J. W. Bozzelli, C.-J. Chen, C. Sheng, and A. M. Dean, *Prepr. Pap. - Am. Chem. Soc., Div. Fuel Chem.* **47**, 219 (2002).

⁴³A. Andersen and E. A. Carter, *J. Phys. Chem. A* **106**, 9672 (2002).

⁴⁴J. D. DeSain, S. J. Klippenstein, J. A. Miller, and C. A. Taatjes, *J. Phys. Chem. A* **107**, 4415 (2003).

⁴⁵H.-H. Carstensen, C. V. Naik, and A. M. Dean, *J. Phys. Chem. A* **109**, 2264 (2005).

⁴⁶H. Hippler and B. Viskolcz, *Phys. Chem. Chem. Phys.* **2**, 3591 (2000).

⁴⁷G. L. Vaghjiani and A. R. Ravishankara, *J. Phys. Chem.* **93**, 1948 (1989).

⁴⁸D. L. Osborn, H. Choi, D. H. Mordant, R. T. Bise, and D. M. Neumark, *J. Chem. Phys.* **106**, 3049 (1997).

⁴⁹A. W. Harrison, M. Ryazanov, E. N. Sullivan, and D. M. Neumark, *J. Chem. Phys.* **145**, 024305 (2016).

⁵⁰D. Irimia, D. Dobrikov, R. Kortekaas, H. Voet, D. A. van dan Ende, W. A. Groen, and M. H. M. Janssen, *Rev. Sci. Instrum.* **80**, 113303 (2009).

⁵¹D. Irimia, R. Kortekaas, and M. H. M. Janssen, *Phys. Chem. Chem. Phys.* **11**, 3958 (2009).

⁵²J. M. B. Bakker, *J. Phys. E* **6**, 785 (1973).

⁵³J. M. B. Bakker, *J. Phys. E* **7**, 364 (1974).

- ⁵⁴V. Dribinski, A. Ossadtschi, V. A. Mandelshtam, and H. Reisler, *Rev. Sci. Instrum.* **73**, 2634 (2002).
- ⁵⁵O. Jagutzki, A. Cerezo, A. Czasch, R. Dörner, M. Hattas, M. Huang, V. Mergel, U. Spillmann, K. Ullmann-Pflegler, T. Weber, H. Schmidt-Böcking, and G. D. W. Smith, *IEEE Trans. Nucl. Sci.* **49**, 2477 (2002).
- ⁵⁶A. W. Harrison, J. S. Lim, M. Ryazanov, G. Wang, S. Gao, and D. M. Neumark, *J. Phys. Chem. A* **117**, 11970 (2013).
- ⁵⁷R. N. Zare, *Mol. Photochem.* **4**, 1 (1972).
- ⁵⁸V. A. Mozhayskiy and A. I. Krylov, ezSpectrum3.0, iOpenShell Center for Computational Studies of Electronic Structure and Spectroscopy of Open Shell and Electronically Excited Species, Los Angeles, <http://iopenshell.usc.edu/downloads>.
- ⁵⁹M. J. Frisch, G. W. Trucks, H. B. Schlegel, G. E. Scuseria, M. A. Robb, J. R. Cheeseman, G. Scalmani, V. Barone, V. Mennucci, G. A. Petersson, H. Nakatsuji, M. Caricato, S. Li, H. P. Hratchian, A. F. Izmaylov, J. Bloino, G. Zheng, J. L. Sonnenberg, M. Hada, M. Ehara, K. Toyota, R. Fukuda, J. Hasegawa, M. Ishida, T. Nakajima, Y. Honda, O. Kitao, H. Nakai, T. Vreven, J. A. Montgomery, J. E. Peralta, F. Ogliaro, M. Bearpark, J. J. Heyd, E. Brothers, K. N. Kudin, V. N. Staroverov, T. Keith, R. Kobayashi, J. Normand, K. Raghavachari, A. Rendell, J. C. Burant, S. S. Iyengar, J. Tomasi, M. Cossi, N. Rega, J. M. Millam, M. Klene, J. E. Knox, J. B. Cross, V. Bakken, C. Adamo, J. Jaramillo, R. Gomperts, R. E. Stratmann, O. Yazyev, A. J. Austin, R. Cammi, C. Pomelli, J. W. Ochterski, R. L. Martin, K. Morokuma, V. G. Zakrzewski, G. A. Voth, P. Salvador, J. J. Dannenberg, S. Dapprich, A. D. Daniels, O. Farkas, J. B. Foresman, J. V. Ortiz, J. Cioslowski, and D. J. Fox, GAUSSIAN 09, Revision C.01, Gaussian, Inc., Wallingford, CT, USA, 2009.
- ⁶⁰M. P. Andersson and P. Uvdal, *J. Phys. Chem. A* **109**, 2937 (2005).
- ⁶¹D. E. Szpunar, A. E. Faulhaber, K. E. Kautzman, P. E. Crider II, and D. M. Neumark, *J. Chem. Phys.* **126**, 114311 (2007).
- ⁶²M. Ryazanov, A. W. Harrison, G. Wang, P. E. Crider, and D. M. Neumark, *J. Chem. Phys.* **140**, 234304 (2014).
- ⁶³D. L. Osborn, D. J. Leahy, and D. M. Neumark, *J. Phys. Chem. A* **101**, 6583 (1997).
- ⁶⁴D. Cyr, D. Leahy, D. Osborn, R. Continetti, and D. M. Neumark, *J. Chem. Phys.* **99**, 8751 (1993).
- ⁶⁵G. J. Vazquez, S. D. Peyerimhoff, and R. J. Buenker, *Chem. Phys.* **99**, 239 (1985).
- ⁶⁶A. V. Copan, H. F. Schaefer III, and J. Agarwal, *Mol. Phys.* **113**, 2992 (2015).
- ⁶⁷R. A. Bair and W. A. Goddard III, *J. Am. Chem. Soc.* **104**, 2719 (1982).
- ⁶⁸R. A. Marcus and O. K. Rice, *J. Phys. Chem.* **55**, 894 (1951).
- ⁶⁹T. Beyer and D. F. Swinehart, *Commun. ACM* **16**, 379 (1973).
- ⁷⁰C. Maul and K.-H. Gericke, *Int. Rev. Phys. Chem.* **16**, 1 (1997).
- ⁷¹P. E. Crider, A. W. Harrison, and D. M. Neumark, *J. Chem. Phys.* **134**, 134306 (2011).
- ⁷²N. Neumann, D. Hant, L. P. Schmidt, J. Titze, T. Jahnke, A. Czasch, M. S. Schöffler, K. Kreidi, O. Jagutzki, H. Schmidt-Böcking, and R. Dörner, *Phys. Rev. Lett.* **104**, 103201 (2010).
- ⁷³B. B. Shen, B. L. J. Poad, and R. E. Continetti, *J. Phys. Chem. A* **118**, 10223 (2014).
- ⁷⁴E. P. Clifford, P. G. Wenthold, R. Gareyev, W. C. Lineberger, C. H. Depuy, V. M. Bierbaum, and G. B. Ellison, *J. Chem. Phys.* **109**, 10293 (1998).
- ⁷⁵D. F. McMillen and D. M. Golden, *Annu. Rev. Phys. Chem.* **33**, 493 (1982).